

Tuning Halide Composition Allows Low Dark Current Perovskite Photodetectors With High Specific Detectivity

Francesco Furlan, Davide Nodari, Emanuele Palladino, Edoardo Angela, Lokeshwari Mohan, Joe Briscoe, Matthew J. Fuchter, Thomas J. Macdonald, Giulia Grancini, Martyn A. McLachlan, and Nicola Gasparini*

Tuning halide composition in perovskites is a powerful approach demonstrated to enhance the performance of perovskite photovoltaic devices where such compositional modifications drive improvements in open-circuit voltage (V_{oc}) and a reduction in nonradiative voltage losses. Similarly, photodetectors (PDs) operate as light to current conversion devices hence it is relevant to investigate whether performance enhancements can be achieved by similar strategies. Herein, perovskite PDs are fabricated with an inverted photo-diode configuration based on a $\text{MAPb}(\text{I}_{1-x}\text{Br}_x)_3$ perovskite (MA = methylammonium) active layer over the $x = 0\text{--}0.25$ composition range. Interestingly, it has been found that increasing the Br content up to 0.15 (15%) leads to a significant reduction in dark current (J_d), with values as low as $1.3 \times 10^{-9} \text{ A cm}^{-2}$ being achieved alongside a specific detectivity of 8.7×10^{12} Jones. Significantly, it has been observed an exponential relationship between the J_d of devices and their V_{oc} over the 0–15% Br range. The superior performances of the 15% Br-containing devices are attributed to the reduction of trap states, a better charge extraction of photogenerated carriers, and an improvement in photoactive layer morphology and crystallinity.

interest in both academic and industrial landscapes for a wide range of applications, including image sensing,^[8] optical communication,^[9] environmental monitoring, and biomedical applications.^[10,11] New emerging applications require self powered, cost-effective, highly sensitive, and flexible devices.^[12–14] These conditions can be fully satisfied using PDs based on perovskite active layers, which combine high ambipolar charge carrier mobility^[6,15] with long carrier diffusion length,^[16,17] effective light absorption,^[18] high defect tolerance^[19,20] and low-cost solution processability,^[21] making them suitable candidates for high-performance PDs.

The route to obtain highly sensitive sensors requires minimizing dark current (J_d) values, which limits the noise (i_n) in devices and maximizes light conversion. To date, few methods exist to reduce the dark current in PDs. They are based on the use of charge-blocking


layers to minimize charge injection.^[22,23] Other strategies are related to inclusion of additives^[24,25] or controlling film crystallization^[26,27] to minimize backward charge injection at the electrodes. However, there is a deficit of efforts focused on understanding the role of perovskite composition and its correlation to device J_d .

1. Introduction

Organo-metal halide perovskites have gained attention for their remarkable optoelectronic properties, which made them an ideal material for solar cells,^[1–3] light-emitting diodes,^[4] and photodetectors^[5–7] (PDs). PDs are attracting increasing

F. Furlan, D. Nodari, E. Palladino, M. J. Fuchter, T. J. Macdonald, N. Gasparini
 Department of Chemistry and Molecular Sciences Research Hub
 Imperial College London
 White City Campus, 82 Wood Lane, London W12 0BZ, UK
 E-mail: n.gasparini@imperial.ac.uk
 D. Nodari, G. Grancini
 Dipartimento di Chimica and INSTM
 Università di Pavia
 Via T. Taramelli 14, Pavia 27100, Italy

E. Angela, M. A. McLachlan
 Department of Materials
 Imperial College London
 South Kensington Campus, London SW7 2AZ, UK
 L. Mohan, J. Briscoe, T. J. Macdonald
 School of Engineering and Materials Science
 Queen Mary University of London
 London E1 4NS, UK
 M. J. Fuchter, M. A. McLachlan, N. Gasparini
 Centre for Processable Electronics
 Imperial College London
 South Kensington Campus, London SW7 2AZ, UK

 The ORCID identification number(s) for the author(s) of this article can be found under <https://doi.org/10.1002/adom.202201816>.

© 2022 The Authors. Advanced Optical Materials published by Wiley-VCH GmbH. This is an open access article under the terms of the Creative Commons Attribution License, which permits use, distribution and reproduction in any medium, provided the original work is properly cited.

DOI: 10.1002/adom.202201816

In recent years, compositional engineering has played a fundamental role in developing perovskite solar cells, enabling higher device efficiencies, an adjustment of film defect densities, and longer stabilities.^[28–30] Some of the highest performing perovskite solar cells are based on mixed-cation, mixed-halide materials with power conversion efficiencies currently > 25%.^[27,31,32] Incorporating increasing quantities of Br into MAPb(I_{1-x}Br_x)₃ allows effective tuning of the optical bandgap,^[33–37] which is critical to improve the efficiency of both single and multi-junction solar cells.^[38,39] Moreover, altering halide composition can also have positive effects on film crystallization, morphology, and stability.^[36,40] It has been shown that the main loss mechanism in perovskites solar cells is related to the presence of traps, leading to significant nonradiative recombination losses.^[41] The incorporation of small amounts of Br reduces the density of traps with a corresponding positive effect on the electronic quality of the photoactive layer.^[37,42]

In this work, we study the effect of Br doping into methylammonium lead iodide (MAPbI₃) over the composition range of 0–25% Br and report the performance of PDs fabricated with these active layers.

We find that our bandgap engineering increases device open-circuit voltage (V_{oc}) resulting in PDs with significantly reduced J_d values, attributed to improved charge collection efficiency and reduced recombination driven by the Br incorporation.

Furthermore, we obtain an exponential relationship between device J_d and their V_{oc} over the 0–15% Br composition range. We identify the 15% Br, i.e., MAPb(I_{0.85}Br_{0.15})₃ composition as that which creates devices with the lowest J_d values, greatest responsivity, and highest specific detectivity (D^*). The result is PDs with J_d of 1.3×10^{-9} A cm⁻² at -0.5 V and D^* approaching 10^{13} Jones over the 350–730 nm spectral region. Moreover, a wide linear dynamic range, fast frequency response, and transient times are also observed at this specific composition. Thus, halide doping of wide-bandgap perovskites is shown to be a powerful method in the continued development of high-performance PDs.

2. Results and Discussion

A schematic illustration showing the device structure employed is depicted in **Figure 1a**. This architecture and composition were employed for both photovoltaic (PV) and PD devices. Here an inverted architecture employing indium tin oxide (ITO) as a transparent conductive layer and [2-(3,6-dimethoxy-9H-carbazol-9-yl)ethyl]phosphonic acid (MeO-2PACz) as the hole transport layer (HTL), on top of which the perovskite is deposited. The device is then completed with [6,6]-Phenyl-C61-butyric acid methyl ester (PCBM) as the electron transport layer (ETL), bathocuproine (BCP) as the hole blocking layer, and Cu as the top contact. The composition of the perovskite layer investigated is MAPb(I_{1-x}Br_x)₃, over the composition range $x = 0–0.25$, henceforth 0–25%. The optical bandgaps for the different perovskite compositions are extracted from the UV-Vis absorption spectra in **Figure 1b** and the corresponding Tauc plot (**Figure S1**, Supporting Information). As anticipated, a progressive increase in bandgap is seen with increased Br content.^[33–37] Dark current, J_d is a fundamental parameter that heavily

impacts device performance, specifically sensitivity. **Figure 1c** shows current density–voltage ($J–V$) characteristics recorded in the dark and under one sun equivalent illumination. The dark current values were recorded at -0.5 V as lower negative biases can have a negative impact owing to ionic motion.^[43]

In the PV community, it is now widely acknowledged that the small addition of Br onto the MAPb(I_{1-x}Br_x)₃ system is beneficial for enhancing V_{oc} .^[34,37,44] We confirm this behavior in our devices (**Figure 1d**), where we observe a linear increase in V_{oc} over the 0–15% Br composition range, with 15% Br producing the highest V_{oc} values.

Figure 1c and **Figure S2**, Supporting Information show the $J–V$ curves in light and dark conditions for the best PDs over the full 0–25% composition range (**Figure S3**, Supporting Information shows both forward and reverse scans, depicting low hysteresis for all devices). The J_d of the reference device (0% Br) is 2.6×10^{-8} A cm⁻², the addition of 15% Br reduces J_d by an order of magnitude to 1.3×10^{-9} A cm⁻² whilst the 25% devices result in a J_d of 3.0×10^{-7} A cm⁻² (**Figure S4**, Supporting Information depicts the statistical distribution of PD devices) – this is a significant change and highlights the importance of probing more than the intrinsic electronic properties of the active layer (i.e., the bandgap) but also, importantly, the behavior of complete devices. Moreover, both the 0% and 15% show a low variation of the J_d as a function of the applied negative bias, but in the 25% case the dark current varies by almost two orders of magnitude in the voltage region 0 –0.5 V. Interestingly the reduction of J_d in devices operating under reverse bias can be correlated to the increase in the V_{oc} . Our data shows that there is an exponential relationship between the J_d and the V_{oc} , valid up to 15% bromide content. For further bromide addition, the V_{oc} and J_d correlation is lost (**Figure 1d**). This observation is interesting as current literature mainly focuses on the importance of blocking layers and the role of energetics to significantly decrease the J_d values in perovskite PDs.^[22,23] In order to better understand the role of Br addition on perovskite PD performance we investigate the 0, 15, and 25% Br compositions.

In addition to J_d , we evaluate photon-to-electron conversion efficiency by measuring the responsivity (R) of the devices according to Equation 1.

$$R = \frac{EQE\lambda q}{hc} \quad (1)$$

where EQE is the external quantum efficiency, λ is the wavelength of incident light, q is the elementary charge, h is Planck's constant, and c is the speed of light.

The R of the three PDs under applied reverse bias is displayed in **Figure 2a**, with the peak responsivities calculated to be 0.44 A W⁻¹ (700 nm), 0.43 A W⁻¹ (680 nm), and 0.42 A W⁻¹ (680 nm) for 0, 15 and 25% Br respectively. These values are in line with other R -values reported for perovskite PDs.^[45] As expected, the addition of Br results in a blue shift of the responsivity edge position, due to the shift in bandgap. Moreover, the R measured at both 0 V and -0.5 V bias do not show any significant differences (**Figure S5**, Supporting Information), in line with the reported shallow level trap densities for perovskite photoactive layers.^[46]

J_d values and R are usually used to calculate the specific detectivity of PDs, which provides insights into the sensitivity

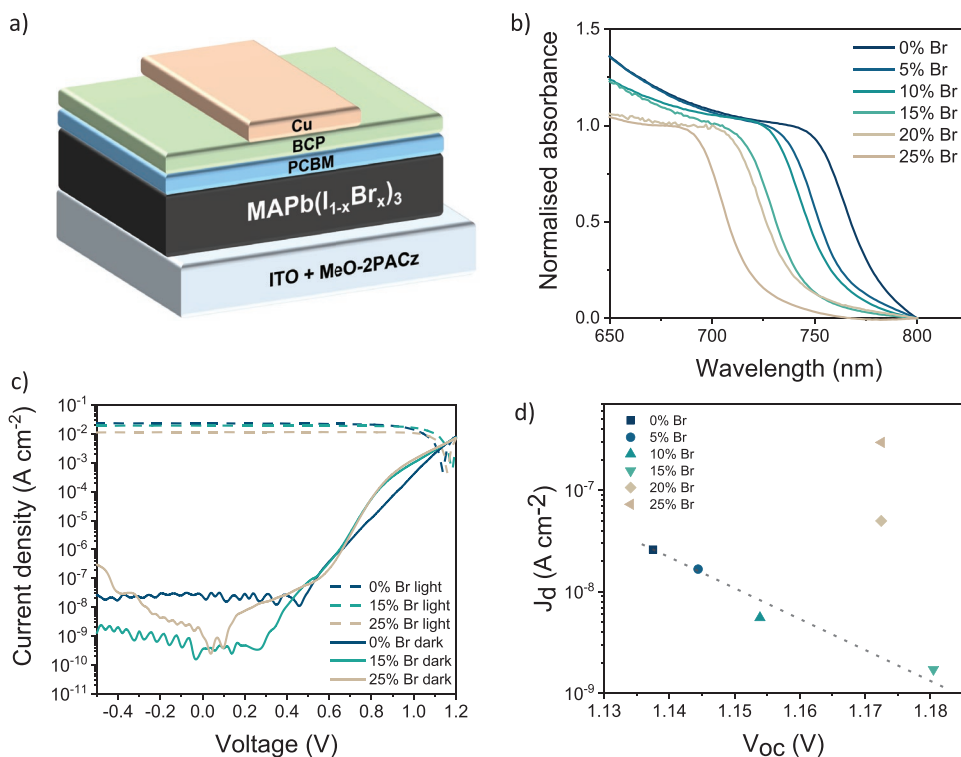


Figure 1. a) Schematic illustration of complete photodetector device structure investigated, b) UV-vis spectra of $\text{MAPb}(\text{I}_{1-x}\text{Br}_x)_3$ over the composition range $x = 0-25$, c) $J-V$ characteristics for 0, 15, and 25% Br inclusion under light (dashed lines) and in dark conditions (solid lines) d) semi-log plot showing an exponential J_d-V_{oc} behavior over the 0–15% Br composition range (V_{oc} extracted at 100 mW cm^{-2} illumination).

of devices (Equation 2). However, it is important to avoid an overestimation of D^* as J_d only considers the shot noise of the device (Figure S6, Supporting Information).^[46] Therefore, here D^* is calculated through the noise current (i_n , Equation 3), which also takes into account the contribution of thermal noise present in all electrical circuits.

$$D^* = \frac{\sqrt{(A\Delta f)R}}{i_n} \quad (2)$$

$$(i_n)^2 = \left(2qi_d + \frac{4kT}{R_{\text{shunt}}} \right) \quad (3)$$

where A is the photodetector area and Δf is the measurement system bandwidth. With R_{shunt} derived from the respective $J-V$ characteristics. The calculated detectivity is shown in Figure 2b. The highest D^* is obtained for the device with a 15% Br addition, $D^* = 8.7 \times 10^{12}$ Jones, while for 0% and 25% Br devices D^* values of 6.0×10^{11} Jones and 1.2×10^{12} Jones respectively are measured. These values are among the highest reported in the literature for D^* calculated with this approach and are promising for applications requiring light detection in the UV-Vis spectral region^[45] (Table S1, Supporting Information). We also measured the noise current spectrum of the devices and the instrument as depicted in Figure S7, Supporting Information. We obtained similar i_n values as calculated from Equation (3)

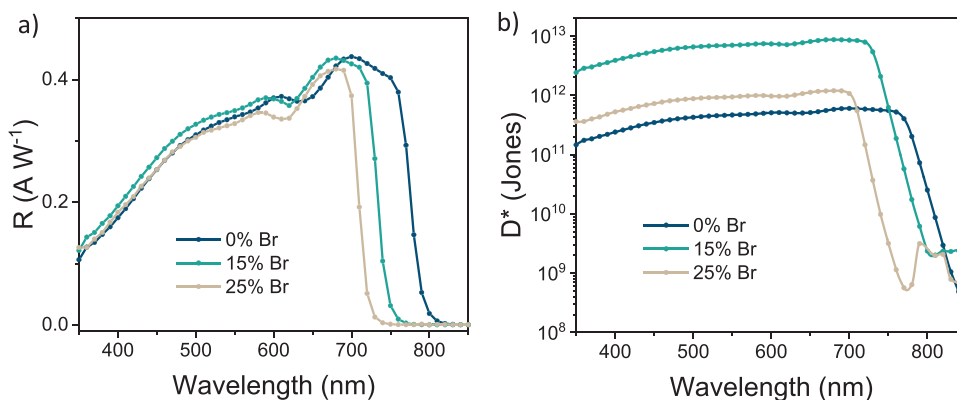


Figure 2. a) Responsivity (R) and b) Specific detectivity (D^*) values for 0, 15, and 25% Br $\text{MAPb}(\text{I}_{1-x}\text{Br}_x)_3$ based photodetectors at -0.5 V .

which justify the high D^* for 15% Br-based PD (Figure S8a,b, Supporting Information).

In addition to high D^* , a linear responsivity over a broad light intensity range is desirable, particularly for applications requiring a high contrast at low light intensities. This property can be extrapolated from linear dynamic range (LDR) measurements, with LDR being related to the photocurrent difference under illumination (J_l) and in dark conditions (J_d) at -0.5 V (Figure 3a). LDR is calculated as:

$$\text{LDR} = 20 \log \left(\frac{J_l}{J_d} \right) \quad (4)$$

In all three cases, a wide linear response is observed as a function of light intensity, with an extended range down to 2.1×10^{-5} mW cm $^{-2}$ for the 15% Br devices, while the linearity is obtained only down to 2.1×10^{-4} mW cm $^{-2}$ and 2.1×10^{-3} mW cm $^{-2}$ for 0 and 25% Br devices respectively. From this trend, LDR values are calculated as 116, 133, and 88 dB for 0, 15, and 25% Br content respectively, at an applied bias of -0.5 V. Another important characteristic for video applications is the response speed, evaluated through the cutoff frequency, which is defined as the photoresponse drop of $1/\sqrt{2}$ of the maximum photocurrent intensity (i_{max}), known as -3 dB limit and calculated as:

$$\text{Damping} = -20 \log \left(\frac{i_{\text{max}}}{i_{\text{freq}}} \right) \quad (5)$$

with i_{freq} being the photocurrent intensity for a specific frequency of light. For video applications, a cutoff frequency of 10 kHz is considered sufficient.^[47] As can be seen from Figure 3b, the lowest cut-off value is 780 Hz for a 25%

bromide content, while they are 60 kHz and 70 kHz for 0% and 15%, respectively. We speculate that the higher performances of the devices containing a 15% Br can be related to an improvement in charge extraction properties and reduced charge carrier recombination. To confirm this hypothesis, a further evaluation of the response speed is carried out by measuring the current transients at -0.5 V under white light illumination at 2 kHz. As shown in Figure 3c and Table 1, rise and fall transient times (defined as the time needed for the signal to rise from 10% to 90% of the maximum signal and fall from 90% to 10%, respectively) for the 15% Br samples are faster when compared to the 0% reference with the values for the 25% Br devices being slower than 15% Br. The superior performance of the 15% Br device is attributed to better charge extraction and reduced charge recombination.^[42,48,49]

Steady-state photoluminescence (PL) measurements are shown in Figure S9, Supporting Information using an excitation of 635 nm and demonstrate a noticeable shift from 775 nm (0% Br) to 725 nm (25% Br), which is consistent with previous reports and indicative of a widening of the bandgap of the absorber material.^[50,51] Time-resolved PL (TRPL) decay kinetics on thin films were analyzed to gain further insight into the recombination mechanisms. An excitation wavelength of 635 nm and a probing wavelength corresponding to the emission maxima were used. The PL decays shown in Figure 3d were fitted with the biexponential function, $\gamma = \gamma_0 + A_1 e^{-\frac{x}{\tau_1}} + A_2 e^{-\frac{x}{\tau_2}}$, where τ_1 represents the surface component (fast decay) and τ_2 represents bulk component (slow decay)^[52,53] (Table S2, Supporting Information). The average lifetimes (τ_{ave}) were calculated as per previous reports^[54,55] where τ_{ave} for 0, 15, and 25% Br were determined to be 80.28, 299.31, and 246.45 ns, respectively. Prolonged τ_{ave} in the perovskite films represents

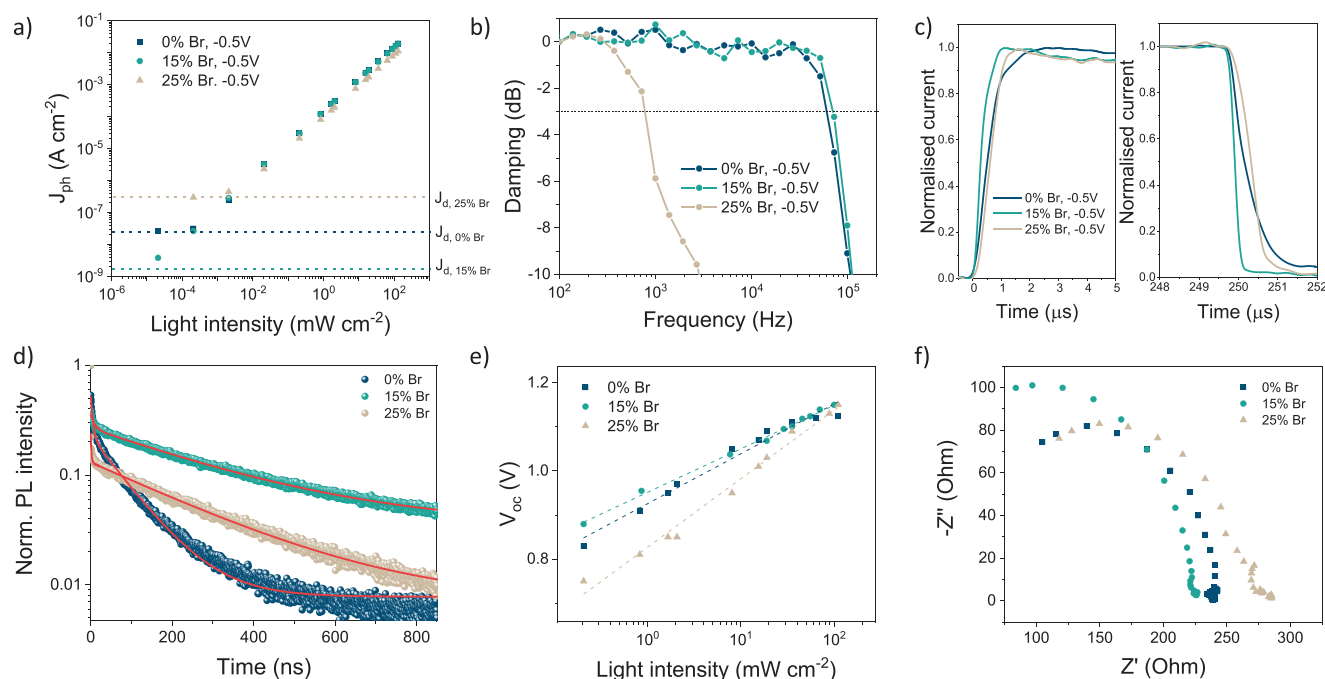


Figure 3. a) Linear dynamic range, b) Cutoff frequency, c) transient photocurrent measurements at -0.5 V, d) TRPL results, e) V_{oc} -light intensity, and f) Impedance spectra for 0, 15, and 25% Br MAPb(I $_{1-x}$ Br $_x$) $_3$ based photodetectors.

Table 1. Rise and fall times, cutoff frequency, and linear dynamic range values for photodetectors based on MAPb(I_{1-x}Br_x)₃ with 0, 15, and 25% Br content, all measured at -0.5 V bias.

Br content [%]	Rise time [μs]	Fall time [μs]	Cutoff frequency [kHz]	LDR [dB]
0	1.08	1.48	60	116
15	0.58	0.17	70	133
25	0.67	0.61	0.78	88

suppressed nonradiative recombination pathways, consistent with the improved efficiency in the 15% Br devices.^[56]

To further elucidate the reasons behind the observed trend in J_d and the V_{oc} , we analyzed the V_{oc} -light intensity trends (Figure 3e). V_{oc} losses in perovskite solar cells are mostly caused by non-radiative recombination induced by the presence of interfaces or trap states within the energy gap.^[57] It is possible to extrapolate the ideality factor n_{id} to evaluate the dominant recombination mechanism in the device, and calculated as:

$$n_{id} = (q/k_b T) (dV_{oc}/d \ln(\Phi)) \quad (6)$$

Values of n_{id} closer to 1 indicate the presence of a good quality active layer with the major recombination events occurring at the interfaces, in contrast for n_{id} is closer to 2 this indicates that the recombination is attributed to the presence of sub-bandgap trap states.^[58] The calculated ideality factors are $1.81kT/q$, $1.59kT/q$ and $2.59kT/q$ for 0, 15 and 25% Br content, respectively. The lower value obtained for the 15% case indicates a lower contribution of trap states to voltage losses and a higher quality perovskite thin film compared to the reference films. Instead, the higher n_{id} value of the 25% film indicates multiple trapping phenomena occurring in the bulk, which contributes significantly to charge recombination events thus reduced device performance.

To understand further the implication of charge recombination on device performance, we carried out impedance spectroscopy measurements.^[59,60] Figure 3f shows the Nyquist plots extracted at 1 sun illumination and V_{oc} conditions. We used the equivalent circuit depicted in Figure S10, Supporting Information, consisting of series resistance (R_s), transport resistance (R_t), recombination resistance (R_{rec}), chemical capacitance (C_μ) and geometrical capacitance (C_g).^[61] We calculated for charge carrier lifetime (τ) and extraction time (t_{ex}) according to Equations 7 and 8, respectively.

$$\tau = R_{rec} \times C_\mu \quad (7)$$

$$t_{ex} = R_t \times C_\mu \quad (8)$$

Generally, PDs with low charge recombination depict τ longer than t_{ex} , i.e., charge carriers can be effectively collected at the electrodes before recombining.^[62,63] In line with their being reduced traps in the 15% Br PDs, we calculate τ and t_{ex} of 4.3 μs and 1.9 μs respectively. The reference devices show identical lifetime and extraction time values (0.7 μs) and the presence of a high concentration of trap states in the 25% Br devices leads to a shorter lifetime (0.6 μs) than extraction time

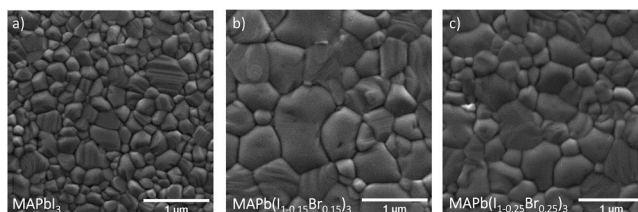


Figure 4. a–c) Surface scanning electron microscopy images MAPb(I_{1-x}Br_x)₃ perovskite thin films

(0.8 μs). Recent works highlighted the importance of the energetic barrier between the perovskite and the hole and electron transporting layers on the thermal charge generation which influences J_d .^[23] Increasing the amount of Bromide enlarges the Eg, which increased the energetic barrier between the conduction band of perovskite and the HOMO level of MeO-2PACz (HTL). However, the lower J_d in 15% Br content of almost two orders of magnitude compared to MAPI-based PD, we believe is due to reduced trap-assisted recombination in addition to the higher energetic barrier. As depicted by our optoelectronic measurements, we observed a significant reduction of trap-assisted recombination, which we believe plays a major role into the reduction of J_d . Given that the reduction of traps via tuning the perovskite composition (15% Br) has an effect on the entire active layer, it is challenging to discriminate whether trap-assisted charge injection or trap-mediated thermal charge generation is the main mechanism underpinning J_d . Differently, when the Br content exceeds 25%, the higher concentration of trap states hindered low J_d values.

The microstructure of the films was studied using scanning electron microscopy. All films show the anticipated polycrystalline morphology, with an increase in grain size observed for the 15 and 25% Br-containing films compared to the 0% reference (Figure 4a–c). Such enhancements of grain size can help reducing nonradiative recombination losses coming from recombination events occurring at the grain boundaries.^[64] X-ray diffraction measurements (Figure S11, Supporting Information) show the expected diffraction patterns consistent with MAPbI₃,^[37,65] from which crystallite size is determined (Table S3, Supporting Information). Similarly, these data show an increase in crystallite size with increased Br content. Despite the 25% Br films exhibiting the highest degree of crystallinity the poor device performance observed is attributed to the higher concentration of trap states introduced by the high Br content.^[41] This conclusion highlights the requirement to balance microstructural improvements with compositional optimization, where strategies may involve cation doping and/or additive engineering such that trap states associate with defects may be passivated thus presenting a viable pathway to further decrease PD J_d values and further extend the range in over which the exponential J_d - V_{oc} relationship is valid.

3. Conclusion

In conclusion, we have demonstrated a facile strategy to reduce the J_d in perovskite PDs. Through tuning the bandgap of the perovskite active layer by compositional engineering, specifically

Br doping in the MAPb(I_{1-x}Br_x)₃ system we produce an optimized device with a D^* of 8.7×10^{12} Jones in the 350–850 nm range and a J_d of 1.3×10^{-9} A cm⁻² at -0.5 V applied bias at a composition of 15% Br. Over the 0–15% Br range, a steady improvement in all PD parameters is seen, specifically improvements in R -values and faster photoresponse than pristine MAPbI₃ films. Moreover, the reduced J_d values can be correlated with the V_{oc} enhancements. Optoelectronic and morphological analyses reveal that improvements in device performance are due to a reduction of nonradiative recombination losses in the perovskite active layer, which are related to a reduction of trap states, a better charge extraction of photogenerated carriers, and an improved morphology of the perovskite thin film. Our results highlight how compositional engineering of the active layer can be an alternative approach to conventional transport layer optimization to improve photodetector performances.

4. Experimental Section

Materials Preparation: Perovskite solution. MAPbI₃ and MAPbBr₃ perovskite precursor solutions were prepared by mixing respectively MAI (Greatcell Solar Materials, >99.99%) with PbI₂ (Alfa Aesar, ultra dry, 99.999%) and MABr (Greatcell Solar Materials, >99.99%) with PbBr₂ (Alfa Aesar, ultra dry, 99.999%) in a 1:1 molar ratio in anhydrous N,N-dimethylformamide (DMF)/dimethyl sulfoxide (DMSO) (9:1 volume ratio) to give a concentration of 1.5 mol L⁻¹. Different quantities of MAPbI₃ and MAPbBr₃ perovskite precursor solutions were then mixed to get the desired MAPb(I_{1-x}Br_x)₃ perovskite composition with x ranging from 0 to 0.25.

Photodetector Fabrication: ITO was ultrasonically cleaned in deionized water, acetone, and isopropanol for 15 min in each solvent. The ITO was then dried with nitrogen and treated by oxygen plasma for 3 min. MeO-2PACz (TCI, >98.0%, 1 mM in ethanol) was then spin-coated on the ITO at 3000 rpm (acceleration of 1500 rpm s⁻¹) for 30 s. The deposition was followed by a 10 min drying step at 100 °C. MAPb(I_{1-x}Br_x)₃ was spin-coated on the HTL at 4000 rpm (acceleration of 4000 rpm s⁻¹) for 20 s, and after 7 s, 0.5 mL of diethyl ether was rapidly dropped on top of the spinning substrate. The substrate was then immediately annealed at 65 °C for 2 min before further annealing at 100 °C for 60 min. After annealing, all films were glassy black and allowed to cool for 10 min before deposition of the ETL. PCBM (Lumtec, >99.5%, 30 mg mL⁻¹ in chlorobenzene) was then spin-coated on top of the perovskite layer at 4000 rpm (acceleration of 4000 rpm s⁻¹) for 20 s. BCP (Lumtec, >99.5%, 0.5 mg mL⁻¹ in methanol) was then spin-coated on top of the PCBM layer at 5000 rpm (acceleration of 4000 rpm s⁻¹) for 20 s. Immediately after BCP was deposited, the substrates were transferred to another glovebox and subject to thermal evaporation. Finally, 100 nm of Cu was thermally evaporated as a top contact at a base pressure of 5×10^{-6} mbar.

Characterizations—J–V Measurements: J–V characteristics were measured using a Keithley 4200 Source-Measure unit (scan rate 25 mV s⁻¹). An Oriel Instruments Solar Simulator with a Xenon lamp and calibrated to a silicon reference cell was used to provide AM1.5G irradiance. For the determination of the LDR, a neutral white light LED driven by a function generator (ThorLabs DC2200) was used. The LED light was attenuated using a selection of neutral density filters placed between the lamp and PPD. The photocurrent (J_{ph}) was calculated as the difference in response between the illuminated current density (J_{light}) and dark current density (J_d) at each light intensity. All the devices were tested in nitrogen atmosphere.

Responsivity: Responsivity was measured using an integrated system from Quantum Design PV300. All the devices were tested in ambient air.

Dynamic Measurements: Dynamic measurements were performed using a digital oscilloscope (Tektronix TDS3032B). The PPDs were illuminated with a neutral white light LED driven by a function generator

(ThorLabs DC2200). For determination of the rise and fall time a 1 kHz square wave pulse was applied to the LED using the function generator. For determination of the cutoff frequency sinusoidal functions with varying frequencies between 100 Hz and 100 kHz were used to drive the LED. All the devices were tested in nitrogen atmosphere.

Spectroscopy Measurements: Absorption spectra were obtained by using a Cary 60 UV-vis Agilent Spectrophotometer. The steady-state PL was carried out using a Horiba FL 1039 and the TRPL measurements were conducted using a Horiba Delta Flex system (detector: PPD-900, Horiba Scientific). A 635 nm laser diode with <200 ps pulse duration (NanoLED N-02B, Horiba Scientific) was used to achieve the excitation with a repetition rate of 1 MHz and a fluence of 0.64 nJ cm⁻² pulse⁻¹. To record the impedance signal, a STAT-I-400 potentiostat of Metrohm LTD was used. The signal was measured starting from 1 MHz down to 0.1 Hz over 50 frequency points, using a potential amplitude of 20 mV, under 100 mW cm⁻² at V_{oc} .

Electron Microscopy: Scanning electron microscopy (SEM) was used to study the morphology of the perovskite layer. SEM images were acquired via an in-lens electron detector using a LEO Gemini 1525 field emission SEM operated at 3 kV.

X-Ray Diffraction: X-ray diffraction (XRD) characterization was employed to investigate the crystal structure of the active material and identify the eventual crystalline phases present in the samples. XRD patterns were obtained using a Bruker D2 Phaser equipped with a Cu-K α source.

Supporting Information

Supporting Information is available from the Wiley Online Library or from the author.

Acknowledgements

F.F. and D.N. contributed equally to this work. G.G. acknowledges the “HY-NANO” project that received funding from the European Research Council (ERC) Starting Grant 2018 under the European Union’s Horizon 2020 research and innovation program (Grant Agreement No. 802862) and the Fondazione Cariplo Economia Circolare 2021 Project “Green flexible hybrid perovskite solar module for the market: from smart lead manipulation to recycling” (FLHYPER, no. 20201067). This project also received funding from the European Commission Research Executive Agency (Grant Agreement Number: 859752 HEL4CHIR-OLED H2020-MSCA-ITN-2019). M.J.F. would like to thank the EPSRC for funding through an Established Career Fellowship (EP/R00188X/1).

Conflict of Interest

The authors declare no conflict of interest.

Data Availability Statement

The data that support the findings of this study are available from the corresponding author upon reasonable request.

Keywords

halide composition, high specific detectivity, low dark current, perovskite photodetectors, trap states

Received: August 3, 2022
Revised: September 8, 2022
Published online:

- [1] S. D. Stranks, H. J. Snaith, *Nat. Nanotechnol.* **2015**, *10*, 391.
- [2] H. J. Snaith, *J. Phys. Chem. Lett.* **2013**, *4*, 3623.
- [3] J.-P. Correa-Baena, M. Saliba, T. Buonassisi, M. Grätzel, A. Abate, W. Tress, A. Hagfeldt, *Science* **2017**, *358*, 739.
- [4] K. Lin, J. Xing, L. N. Quan, F. P. G. de Arquer, X. Gong, J. Lu, L. Xie, W. Zhao, D. Zhang, C. Yan, W. Li, X. Liu, Y. Lu, J. Kirman, E. H. Sargent, Q. Xiong, Z. Wei, *Nature* **2018**, *562*, 245.
- [5] W. Tian, H. Zhou, L. Li, *Small* **2017**, *13*, 1702107.
- [6] L. Dou, Y. M. Yang, J. You, Z. Hong, W. H. Chang, G. Li, Y. Yang, *Nat. Commun.* **2014**, *5*, 5404.
- [7] H. Gu, S. Chen, Q. Zheng, *Adv. Opt. Mater.* **2021**, *9*, 2001637.
- [8] R. Schödel, T. Ott, R. Genzel, R. Hofmann, M. Lehnert, A. Eckart, N. Mouawad, T. Alexander, M. J. Reid, R. Lenzen, M. Hartung, F. Lacombe, D. Rouan, E. Gendron, G. Rousset, A.-M. Lagrange, W. Brandner, N. Ageorges, C. Lidman, A. F. M. Moorwood, J. Spyromilio, N. Hubin, K. M. Menten, *Nature* **2002**, *419*, 694.
- [9] M. Babics, H. Bristow, W. Zhang, A. Wadsworth, M. Neophytou, N. Gasparini, I. McCulloch, *J. Mater. Chem. C* **2021**, *9*, 2375.
- [10] Z. Wu, Y. Zhai, H. Kim, J. D. Azoulay, T. N. Ng, *Acc. Chem. Res.* **2018**, *51*, 3144.
- [11] P. Jacoutot, A. D. Scaccabarozzi, T. Zhang, Z. Qiao, F. Aniés, M. Neophytou, H. Bristow, R. Kumar, M. Moser, A. D. Nega, A. Schiza, A. Dimitrakopoulou-Strauss, V. G. Gregoriou, T. D. Anthopoulos, M. Heeney, I. McCulloch, A. A. Bakulin, C. L. Chochos, N. Gasparini, *Small* **2022**, *18*, 2200580.
- [12] H. Jing, R. Peng, R.-M. Ma, J. He, Y. Zhou, Z. Yang, C.-Y. Li, Y. Liu, X. Guo, Y. Zhu, D. Wang, J. Su, C. Sun, W. Bao, M. Wang, *Nano Lett.* **2020**, *20*, 7144.
- [13] X. Hu, X. Zhang, L. Liang, J. Bao, S. Li, W. Yang, Y. Xie, *Adv. Funct. Mater.* **2014**, *24*, 7373.
- [14] S.-F. Leung, K.-T. Ho, P.-K. Kung, V. K. S. Hsiao, H. N. Alshareef, Z. L. Wang, J.-H. He, *Adv. Mater.* **2018**, *30*, 1704611.
- [15] J. M. Ball, M. M. Lee, A. Hey, H. J. Snaith, *Energy Environ. Sci.* **2013**, *6*, 1739.
- [16] G. Xing, N. Mathews, S. Sun, S. S. Lim, Y. M. Lam, M. Grätzel, S. Mhaisalkar, T. C. Sum, *Science* **2013**, *342*, 344.
- [17] S. D. Stranks, G. E. Eperon, G. Grancini, C. Menelaou, M. J. P. Alcocer, T. Leijtens, L. M. Herz, A. Petrozza, H. J. Snaith, *Science* **2013**, *342*, 341.
- [18] S. De Wolf, J. Holovsky, S. J. Moon, P. Löper, B. Niesen, M. Ledinsky, F. J. Haug, J. H. Yum, C. Ballif, *J. Phys. Chem. Lett.* **2014**, *5*, 1035.
- [19] W.-J. Yin, T. Shi, Y. Yan, *Appl. Phys. Lett.* **2014**, *104*, 063903.
- [20] K. X. Steirer, P. Schulz, G. Teeter, V. Stevanovic, M. Yang, K. Zhu, J. J. Berry, *ACS Energy Lett.* **2016**, *1*, 360.
- [21] M. Cai, Y. Wu, H. Chen, X. Yang, Y. Qiang, L. Han, M. Cai, Y. Wu, L. Han, H. Chen, X. Yang, Y. Qiang, *Adv. Sci.* **2017**, *4*, 1600269.
- [22] S. Yoon, J. Cho, K. M. Sim, J. Ha, D. S. Chung, *Appl. Phys. Lett.* **2017**, *110*, 083301.
- [23] R. Ollearo, J. Wang, M. J. Dyson, C. H. L. Weijtens, M. Fattori, B. T. van Gorkom, A. J. J. M. van Breemen, S. C. J. Meskers, R. A. J. Janssen, G. H. Gelinck, *Nat. Commun.* **2021**, *12*, 7277.
- [24] J. Li, G. Zhang, Z. Zhang, J. Li, Z. Uddin, Y. Zheng, Y. Shao, Y. Yuan, B. Yang, *ACS Appl. Mater. Interfaces* **2021**, *13*, 56358.
- [25] R. Li, J. Peng, Y. Xu, W. Li, L. Cui, Y. Li, Q. Lin, *Adv. Opt. Mater.* **2021**, *9*, 2001587.
- [26] M. Ahmadi, T. Wu, B. Hu, *Adv. Mater.* **2017**, *29*, 1605242.
- [27] T. Du, F. Richeimer, K. Frohna, N. Gasparini, L. Mohan, G. Min, W. Xu, T. J. Macdonald, H. Yuan, S. R. Ratnasingham, S. Haque, F. A. Castro, J. R. Durrant, S. D. Stranks, S. Wood, M. A. McLachlan, J. Briscoe, *Nano Lett.* **2022**, *22*, 979.
- [28] M. Saliba, T. Matsui, J.-Y. Seo, K. Domanski, J.-P. Correa-Baena, M. K. Nazeeruddin, S. M. Zakeeruddin, W. Tress, A. Abate, A. Hagfeldt, M. Grätzel, *Energy Environ. Sci.* **2016**, *9*, 1989.
- [29] M. Saliba, T. Matsui, K. Domanski, J.-Y. Seo, A. Ummadisingu, S. M. Zakeeruddin, J.-P. Correa-Baena, W. R. Tress, A. Abate, A. Hagfeldt, M. Grätzel, *Science* **2016**, *354*, 206.
- [30] N. J. Jeon, J. H. Noh, W. S. Yang, Y. C. Kim, S. Ryu, J. Seo, S. Il Seok, *Nature* **2015**, *517*, 476.
- [31] J. Y. Kim, J.-W. Lee, H. S. Jung, H. Shin, N.-G. Park, *Chem. Rev.* **2020**, *120*, 7867.
- [32] X. Zheng, Y. Hou, C. Bao, J. Yin, F. Yuan, Z. Huang, K. Song, J. Liu, J. Troughton, N. Gasparini, C. Zhou, Y. Lin, D. Xue, B. Chen, A. K. Johnston, N. Wei, M. N. Hedhili, M. Wei, A. Y. Alsalloum, P. Maity, B. Turedi, C. Yang, D. Baran, T. D. Anthopoulos, Y. Han, Z. Lu, O. F. Mohammed, F. Gao, E. H. Sargent, O. M. Bakr, *Nat. Energy* **2020**, *5*, 131.
- [33] L. Gil-Escrig, A. Miquel-Sempere, M. Sessolo, H. J. Bolink, *J. Phys. Chem. Lett.* **2015**, *6*, 3743.
- [34] J. H. Noh, S. H. Im, J. H. Heo, T. N. Mandal, S. Il Seok, *Nano Lett.* **2013**, *13*, 1764.
- [35] G. E. Eperon, S. D. Stranks, C. Menelaou, M. B. Johnston, L. M. Herz, H. J. Snaith, *Energy Environ. Sci.* **2014**, *7*, 982.
- [36] M. I. Dar, M. Abdi-Jalebi, N. Arora, T. Moehl, M. Grätzel, M. K. Nazeeruddin, *Adv. Mater.* **2015**, *27*, 7221.
- [37] M. Daboczi, S. R. Ratnasingham, L. Mohan, C. Pu, I. Hamilton, Y.-C. Chin, M. A. McLachlan, J.-S. Kim, *ACS Energy Lett.* **2021**, *6*, 3970.
- [38] T. Leijtens, K. A. Bush, R. Prasanna, M. D. McGehee, *Nat. Energy* **2018**, *3*, 828.
- [39] D. P. McMeekin, S. Mahesh, N. K. Noel, M. T. Klug, J. C. Lim, J. H. Warby, J. M. Ball, L. M. Herz, M. B. Johnston, H. J. Snaith, *Joule* **2019**, *3*, 387.
- [40] W. Zhang, M. Saliba, D. T. Moore, S. K. Pathak, M. T. Hörantner, T. Stergiopoulos, S. D. Stranks, G. E. Eperon, J. A. Alexander-Webber, A. Abate, A. Sadhanala, S. Yao, Y. Chen, R. H. Friend, L. A. Estroff, U. Wiesner, H. J. Snaith, *Nat. Commun.* **2015**, *6*, 6142.
- [41] S. Mahesh, J. M. Ball, R. D. J. Oliver, D. P. McMeekin, P. K. Nayak, M. B. Johnston, H. J. Snaith, *Energy Environ. Sci.* **2020**, *13*, 258.
- [42] S. Wheeler, D. Bryant, J. Troughton, T. Kirchartz, T. Watson, J. Nelson, J. R. Durrant, **2017**, *121*, 13496.
- [43] L. Bertoluzzi, J. B. Patel, K. A. Bush, C. C. Boyd, R. A. Kerner, B. C. O'Regan, M. D. McGehee, *Adv. Energy Mater.* **2021**, *11*, 2002614.
- [44] Y. Tu, J. Wu, Z. Lan, X. He, J. Dong, J. Jia, P. Guo, J. Lin, M. Huang, Y. Huang, *Sci. Rep.* **2017**, *7*, 44603.
- [45] L. Li, S. Ye, J. Qu, F. Zhou, J. Song, G. Shen, *Small* **2021**, *17*, 2005606.
- [46] W. L. Leong, Z.-E. Ooi, D. Sabba, C. Yi, S. M. Zakeeruddin, M. Graetzel, J. M. Gordon, E. A. Katz, N. Mathews, *Adv. Mater.* **2016**, *28*, 2439.
- [47] R. D. Jansen-van Vuuren, A. Armin, A. K. Pandey, P. L. Burn, P. Meredith, *Adv. Mater.* **2016**, *28*, 4766.
- [48] X. Zheng, J. Troughton, N. Gasparini, Y. Lin, M. Wei, Y. Hou, J. Liu, K. Song, Z. Chen, C. Yang, B. Turedi, A. Y. Alsalloum, J. Pan, J. Chen, A. A. Zhumekenov, T. D. Anthopoulos, Y. Han, D. Baran, O. F. Mohammed, E. H. Sargent, O. M. Bakr, *Joule* **2019**, *3*, 1963.
- [49] F. H. Isikgor, F. Furlan, J. Liu, E. Ugur, M. K. Eswaran, A. S. Subbiah, E. Yengel, M. De Bastiani, G. T. Harrison, S. Zhumagali, C. T. Howells, E. Aydin, M. Wang, N. Gasparini, T. G. Allen, A. ur Rehman, E. Van Kerschaver, D. Baran, I. McCulloch, T. D. Anthopoulos, U. Schwingenschlögl, F. Laquai, S. De Wolf, *Joule* **2021**, *5*, 1566.
- [50] C. Lin, J. Lee, J. Kim, T. J. Macdonald, J. Ngiam, B. Xu, M. Daboczi, W. Xu, S. Pont, B. Park, H. Kang, J. Kim, D. J. Payne, K. Lee, J. R. Durrant, M. A. McLachlan, *Adv. Funct. Mater.* **2020**, *30*, 1906763.
- [51] K. A. Bush, K. Frohna, R. Prasanna, R. E. Beal, T. Leijtens, S. A. Swifter, M. D. McGehee, *ACS Energy Lett.* **2018**, *3*, 428.
- [52] T. J. MacDonald, A. J. Clancy, W. Xu, Z. Jiang, C. T. Lin, L. Mohan, T. Du, D. D. Tune, L. Lanzetta, G. Min, T. Webb, A. Ashoka, R. Pandya, V. Tileli, M. A. McLachlan, J. R. Durrant, S. A. Haque, C. A. Howard, *J. Am. Chem. Soc.* **2021**, *143*, 21549.

- [53] D. Shi, V. Adinolfi, R. Comin, M. Yuan, E. Alarousu, A. Buin, Y. Chen, S. Hoogland, A. Rothenberger, K. Katsiev, Y. Losovyj, X. Zhang, P. A. Dowben, O. F. Mohammed, E. H. Sargent, O. M. Bakr, *Science* **2015**, *347*, 519.
- [54] A. S. R. Bati, M. Hao, T. J. Macdonald, M. Batmunkh, Y. Yamauchi, L. Wang, J. G. Shapter, *Small* **2021**, *17*, 2101925.
- [55] N. Fu, C. Huang, P. Lin, M. Zhu, T. Li, M. Ye, S. Lin, G. Zhang, J. Du, C. Liu, B. Xu, D. Wang, S. Ke, *J. Mater. Chem. A* **2018**, *6*, 8886.
- [56] R. Cheng, C. Chung, H. Zhang, F. Liu, W. Wang, Z. Zhou, S. Wang, A. B. Djurišić, S. Feng, *Adv. Energy Mater.* **2019**, *9*, 1901980.
- [57] E. Aydin, M. Bastiani, S. Wolf, *Adv. Mater.* **2019**, 1900428, 1900428.
- [58] P. Caprioglio, C. M. Wolff, O. J. Sandberg, A. Armin, B. Rech, S. Albrecht, D. Neher, M. Stollerfoht, *Adv. Energy Mater.* **2020**, *10*, 2000502.
- [59] G. Garcia-Belmonte, A. Munar, E. M. Barea, J. Bisquert, I. Ugarte, R. Pacios, *Org. Electron.* **2008**, *9*, 847.
- [60] Y. Hou, S. Scheiner, X. Tang, N. Gasparini, M. Richter, N. Li, P. Schweizer, S. Chen, H. Chen, C. O. R. Quiroz, X. Du, G. J. Matt, A. Osvet, E. Spiecker, R. H. Fink, A. Hirsch, M. Halik, C. J. Brabec, *Adv. Mater. Interfaces* **2017**, *4*, 1700007.
- [61] J. Bisquert, L. Bertoluzzi, I. Mora-sero, G. Garcia-belmonte, *J. Phys. Chem. C* **2014**, *118*, 18983.
- [62] G. D. Spyropoulos, C. O. Ramirez Quiroz, M. Salvador, Y. Hou, N. Gasparini, P. Schweizer, J. Adams, P. Kubis, N. Li, E. Spiecker, T. Ameri, H. Egelhaaf, C. J. Brabec, *Energy Environ. Sci.* **2016**, *9*, 2302.
- [63] N. Gasparini, S. Righi, F. Tinti, A. Savoini, A. Cominetti, R. Po, N. Camaioni, *ACS Appl. Mater. Interfaces* **2014**, *6*, 21416.
- [64] T. Du, S. R. Ratnasingham, F. U. Kosasih, T. J. Macdonald, L. Mohan, A. Augurio, H. Ahli, C. Lin, S. Xu, W. Xu, *Adv. Energy Mater.* **2021**, *11*, 2101420.
- [65] T. Du, J. Kim, J. Ngiam, S. Xu, P. R. F. Barnes, J. R. Durrant, M. A. McLachlan, *Adv. Funct. Mater.* **2018**, *2*, 1801808.